Volume 13
Number 9
7 March 2025
Pages 6107–6848

Journal of Materials Chemistry A

Materials for energy and sustainability

rsc.li/materials-a

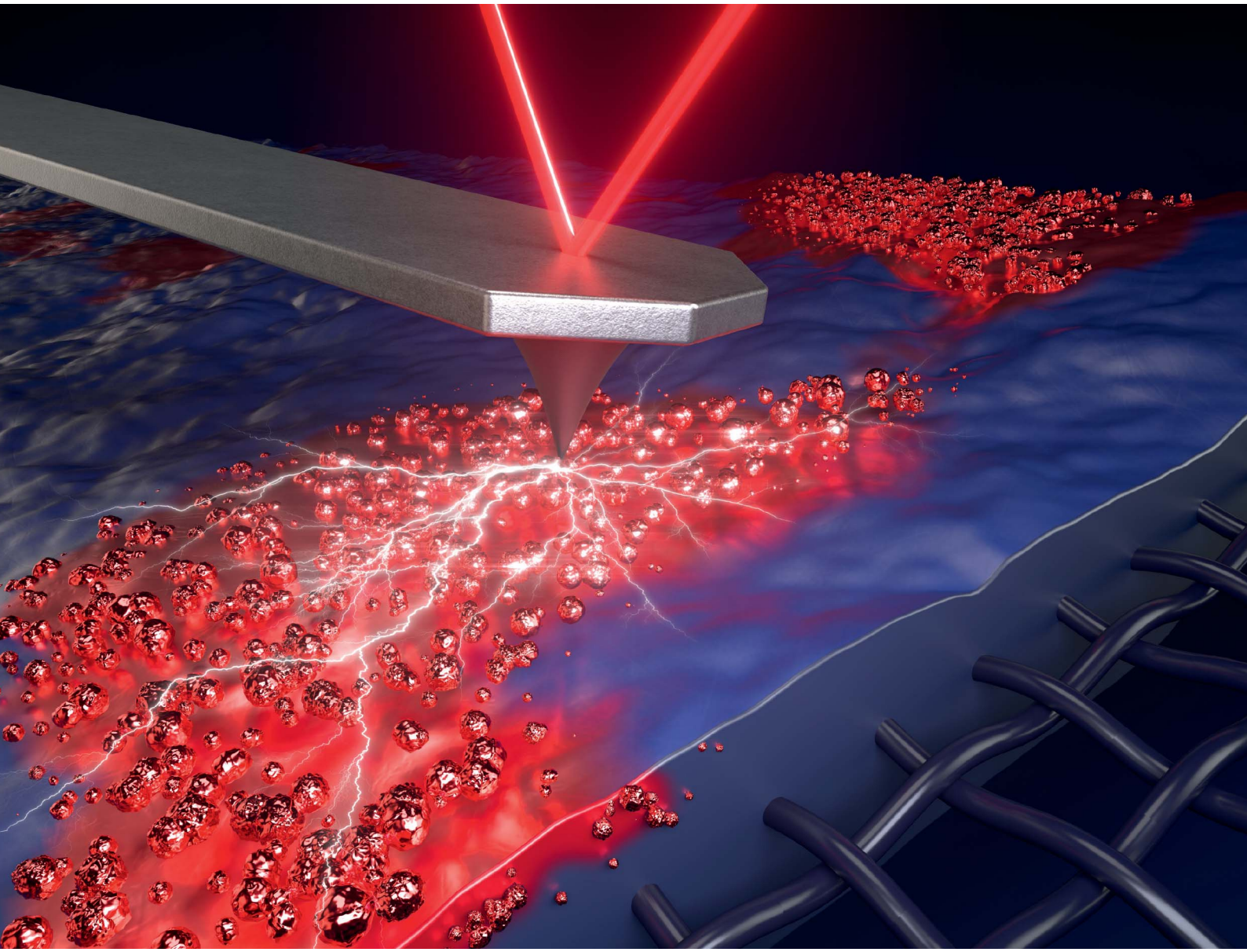

ISSN 2050-7488

ROYAL SOCIETY OF CHEMISTRY

PAPER

Julian Borowec, Florian Hausen *et al.*
Nanomechanical and nanoelectrical analysis of the proton exchange membrane water electrolyzer anode – impact of reinforcement fibers and porous transport layer

Journal of Materials Chemistry A

ROYAL SOCIETY OF CHEMISTRY

PAPER

View Article Online
View Journal | View Issue

Cite this: J. Mater. Chem. A, 2025, 13, 6347

Nanomechanical and nanoelectrical analysis of the proton exchange membrane water electrolyzer anode – impact of reinforcement fibers and porous transport layer†

Julian Borowec, *[ab] Lukas Rein, [ab] Nelli Gorin,[ab] Shibabrata Basak, [a] Ladislaus Dobrenizki,[c] Günter Schmid, [c] Eva Jodat, [a] André Karl, [a] Rüdiger-A. Eichel [ab] and Florian Hausen *[ab]

Understanding the aging of proton exchange membrane electrolyzer cells (PEMECs) is essential for durability enhancement. Therefore, a large-scale and long-term operated (>5000 h) web-woven reinforced membrane electrode assembly (MEA) anode was investigated using nanomechanical and nanoelectrical atomic force microscopy (AFM) techniques and nanoindentation. Web-woven fibers locally increase the reduced modulus and hardness and proved to be a suitable reinforcement for long-term operation. Interestingly, both pristine and operated anodes show slightly diminished electrically conductive surface areas above reinforcement fiber intersections. The homogeneous pristine anode heterogenizes with operation. Additional porous transport layer (PTL) related domains and increased statistical deviations are observed. Nanoindentation revealed a generally increased reduced modulus and hardness with operation, accompanied by a stiffening of the near surface catalyst shown by AFM. This effect is promoted by a loss of low stiffness ionomer, confirmed by the increase of electrically conductive anode surface area. The most significant anode aging effects were observed only at a small surface fraction—at certain PTL related marks. This study firstly analyzes a web-woven fiber reinforced MEA and enhances the understanding of anode aging related to reinforcement fibers and PTL.

Received 15th October 2024
Accepted 16th December 2024

DOI: 10.1039/d4ta07367c

rsc.li/materials-a

1 Introduction

Membrane electrode assemblies (MEAs) are the core of proton exchange membrane electrolyzer cells (PEMECs) and their optimization is crucial for the efficient production of green hydrogen. Durability is the most critical constraint for the PEMEC commercialization as it relates to the cost and reliability.[1] PEMEC's harsh acidic and oxidative environment requires costly precious metal catalysts,[2–4] and affect the MEA and other components.[5] Postmortem analysis of the cell stacks revealed that utilized membranes were the weakest parts in a PEMEC regarding the long-term performance.[6,7] The performance decay and durability restriction of membranes are attributed to membrane poisoning,[8] chemical (*e.g.* hydrogen peroxide related radical attack),[9–11] thermal,[12] or mechanical degradation.[13] Especially, the complete immersion in water results in an increased swelling and a decrease of the mechanical strength and integrity.[1] Recent reports even highlighted the use of thinner membranes, yielding lower ohmic resistance and thus, allowing higher current densities to achieve higher electrolysis efficiency.[14] As a downside, utilization of thin membranes increases the gas crossover and lowers the mechanical strength. The lower mechanical strength of thin membranes is overcome by the utilization of membrane reinforcements.[15–18] Apart from covalent membrane crosslinking,[19] materials such as woven web structures,[20] expanded polytetrafluoroethylene (ePTFE) layers,[21–23] PTFE fibers,[24] electrospun fibers,[25,26] glass-fibers,[27] or various others are utilized as integrated reinforcement. Beside the typical tensile tests,[28–30] MEA's or membrane's mechanics are alternatively characterized by high resolution advanced methods, such as nanoindentation,[31–35] or force–distance curve based atomic force microscopy (AFM) techniques.[22,23,36–42] While there are many reports on proton exchange membrane fuel cell (PEMFC) MEAs, only a few force–distance curve based AFM studies are present for PEMEC MEAs.[43,44] In one of these studies the authors report a loss of ionomer and catalyst in the anode after high current density operation.[43] Ir catalyst loss was reported to occur to an extent due to dissolution and reprecipitation after migrating through the

[a]Institute of Energy Technologies - Fundamental Electrochemistry (IET-1), Forschungszentrum Jülich GmbH, 52425 Jülich, Germany. E-mail: j.borowec@fz-juelich.de; f.hausen@fz-juelich.de

[b]Institute of Physical Chemistry, RWTH Aachen University, 52074 Aachen, Germany

[c]SE TI SES PRM (Sustainable Energy Solutions - Product - Management), Siemens Energy Global GmbH & Co. KG, 91058 Erlangen, Germany

† Electronic supplementary information (ESI) available. See DOI: https://doi.org/10.1039/d4ta07367c

membrane on the cathode.[45] Moreover, the catalyst loss is also associated with ionomer loss,[1] which serves as a catalyst binder. In another PEMEC study, utilization of a coated PTL resulted in a reduced ionomer loss and a reduced restructuring of the anode, indicating the importance of the interface of porous transport layer (PTL) and catalyst layer.[44]

In this work, for the first time a web-woven fiber reinforced PEMEC MEA anode, which was long-term operated (>5000 h), is investigated by means of nanoindentation and PeakForce tunneling atomic force microscopy (PF-TUNA),[46,47] a current sensing and force–distance curve based AFM mode. The anode's nanomechanical and nanoelectrical properties with respect to its unique structural features are analyzed. As anode PTL a Ti hierarchically structured metal grid was utilized, which is favourable due to low manufacturing costs,[48,49] and no need for additional flow fields. At weld seems of the hierarchically structured anode PTL, the cross-formation of crystalline Ir filaments was reported on the same MEA as herein investigated. These filaments, initiated at the anode, grew towards the cathode and, might ultimately sap efficiency due to parasitic currents.[50] The goal of this study is to resolve the interplay of web-woven reinforcement fibers and the PTL with the anode to understand local aging phenomena and thereby, contribute to the rational design of efficient PEMECs.

2 Experimental section

2.1 Membrane electrode assembly

The for laboratory purpose prepared large-scale MEA sample was taken out from a MW-scale research test-bench using a full-size sample module specifically manufactured for durability testing. The proprietary MEA was provided by Siemens Energy consisting of a reinforced perfluorosulfonic acid (PFSA) membrane with a Pt-based cathode and an Ir-based anode. Operation hours were cumulated over more than 5000 h with an arbitrary operation profile given by the availability of cheap electricity including more than 150 cycles of load changes with varying intensity. The cell voltage was below 2 V after the stop of the durability test run. A Ti hierarchically structured expanded metal grid was used as PTL on the anode (see Fig. S1†). Pristine and operated MEAs were cut at equivalent positions for analysis. The cut samples were positioned equally distanced from water inflow and outflow (see Fig. S2†). Furthermore, two pieces, equally distanced from the MEA center were analyzed to enhance the statistics. Operated samples were dried in ambient air for more than seven days before characterization. The anodes of the pristine and long-term operated MEAs are subsequently referred to as pristine and operated anodes.

2.2 Ion beam polishing

A MEA cross section was ion beam polished with an IB-19530CP (JEOL, Japan). To minimize thermal damage of the membrane,[51] the polishing was performed at −120 °C. An acceleration voltage of 3 kV, resulting in a sensed current of around 10 μA, was applied for a duration of 26 h.

2.3 Scanning electron microscopy and energy dispersive spectroscopy

Scanning Electron Microscopy (SEM) investigation was performed with an AMBER X (TESCAN, Czech Republic) at high vacuum mode and room temperature. 1 cm × 1 cm samples fixed with conductive carbon tape were imaged with a Field of View (FoV) of 1.5 mm using the secondary electron detector (Everhardt–Thernley, E–T) detector with a beam acceleration of 5 keV and a beam current of 300 pA at a scan speed of 4 μs. Energy Dispersive Spectroscopy (EDS) was conducted utilizing a 70 mm^2 Elite Super EDS detector (EDAX, USA) integrated within the AMBER X system. The acquired data was analyzed using the EDAX Apex Advanced Software suite. The FoVs of the elemental maps are 180 μm with a resolution of 125.7 eV. Compared to SEM, the beam acceleration was changed to 20 keV with a beam current of 3 nA.

2.4 Nanoindentation

The nanoindentations were performed with a Hysitron TI 980 (Bruker, USA) with a Berkovich tip at ambient conditions. 1 cm × 1 cm samples were cut and glued with cyanoacrylate glue onto a stainless steel substrate ensuring there was no air between MEA and substrate. 360 μm × 360 μm maps were acquired by performing 18 × 18 indents with 20 μm spacing between each indent, preventing an overlap of indented areas. Indents were performed force controlled with constant load and unload rates of 160 μN s^{-1} for 5 s. The resulting maximum load of 800 μN was hold constant for 2 s in between unload and load phases. Reduced modulus and hardness were determined by TriboScan Analysis software (Bruker, USA) with the Oliver–Pharr Model.[52] The individual indents were categorized based on optical microscope images (see Fig. S3–5†). Reduced modulus and hardness of indents of the same domain type were subsequently averaged.

2.5 PeakForce tunneling atomic force microscopy

AFM measurements were performed with a Dimension Icon (Bruker, USA) in the current sensing and force–distance curve based PeakForce tunneling atomic force microscopy mode (PF-TUNA, Bruker, USA) at ambient conditions. The cathode side was mounted with double sided tape onto a steel disc. Additional conductive carbon tape, mounted on top of one anode side of the 1 cm^2 samples, ensured good electrical contact. The applied bias voltage was 20 mV and the current sensitivity was 1 nA V^{-1}. PPP-NCSTPt cantilevers (Nanosensors, Switzerland) with determined spring constants between 16 N m^{-1} to 20 N m^{-1} and an electrically conductive $PtIr_5$ coating on the silicon tip have been individually calibrated performing five ramps onto a sapphire sample (Bruker, USA). The deflection sensitivities and spring constants were calculated using the Nanoscope software (9.4r2, Bruker, USA) from the retraction part of each ramp and averaged. 5 μm × 5 μm maps for statistical analysis were measured with a constant maximum normal load of 40 nN and a slow scan rate of 0.3 Hz. The scans consists of 256 × 256 Pixels. The recorded contact

current is the current averaged over the tip-sample contact duration during each tapping cycle. The 0.5 μm × 0.5 μm high resolution scan was acquired with a scan rate of 0.5 Hz, while the residual parameters were the same as for the 5 μm × 5 μm maps. The stiffness was calculated from the force–distance curves with the Derjaguin, Muller, Toporov (DMT) model.[53] To recalculate the tip radius, which is needed for DMT model calculations,[54] the polystyrene of the PS-LDPE-12M sample (Bruker, USA) with a nominal stiffness of 2 GPa was utilized as reference. The stiffness histograms were derived from analysis of the 5 μm × 5 μm stiffness maps and display the pixel counts and their respective stiffness. The classification was performed with 200 bins, with logarithmically equal size, between 10 MPa to 5000 MPa. As a basis for the AFM data processing, the pySPM package (v0.2.20) for python was utilized.[55] The shown 0.5 μm × 0.5 μm topography map was Gaussian filtered and first order slope corrected. All shown typography maps were first order slope corrected.

3 Results and discussion

3.1 Cross section of a web-woven fiber reinforced MEA

To evaluate the influence of reinforcement fibers on the local anode aging, their location and properties were first analyzed within the pristine MEA's bulk. Fig. 1a shows an optical microscope image of an ion beam polished pristine MEA cross section, exhibiting the catalyst coated ionomer membrane with protective foils (KAPTON®) on both, anode (top) and cathode (bottom) side. The ionomer membrane exhibits three fibers of circular cross-sectional dimensions which point into the image plane. Another fiber is in plane with the cross section, passing the orthogonal oriented fibers below and above in an alternating pattern, indicating the web-woven structure. Fig. 1b–d exhibit the PF-TUNA topography, stiffness and contact current map of the area, which is indicated by the dashed box in Fig. 1a. From bottom to top, the reinforcement fiber, the ionomer, the catalyst layer, and a small part of the protective foil are displayed. The stiffness map in Fig. 1c reveals the mechanical properties of the MEA components (fiber, ionomer, catalyst layer). The ionomer membrane exhibits the least, the catalyst layer an increased, and the reinforcement fiber the highest stiffness. Fig. 1d shows the simultaneously acquired contact current map, clearly indicating, that only the catalyst layer is electrically conductive, while the ionomer and the reinforcement fibers are electrically non-conductive. The scheme in Fig. 1e indicates the top view structure of the web-woven reinforcement fibers. Cross sectioning a MEA at a spot such as indicated with A–A, results in the schematical depiction in Fig. 1f, which represents the right side of the optical microscope image (Fig. 1a).

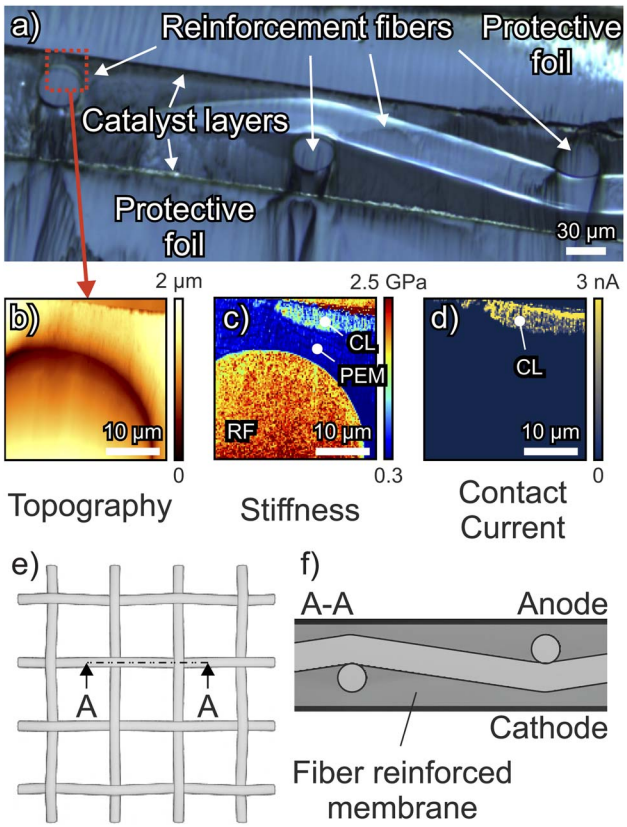

Fig. 1 (a) An ion beam polished cross section of a pristine MEA exhibits the web-woven structure of reinforcement fibers in the bulk of the ionomer membrane. (b–d) The PF-TUNA maps were acquired at the dashed box, indicated in (a), and reveal the topography, the stiffness, and the contact current maps of an area with reinforcement fiber (RF), proton exchange membrane (PEM), anode catalyst layer (CL), and a small part of the protective foil. The reinforcement fiber exhibits a much higher stiffness compared to the ionomer membrane and the catalyst layer. An electrical current is only observed at the anode's catalyst layer. (e) The scheme indicates the top view structure of the membrane's web-woven reinforcement fibers. (f) The cross section A–A of a fiber reinforced MEA, located at a position such as indicated in (e), represents a comparable scheme of the right side of the optical microscope image (a).

3.2 Scanning electron microscopy analysis

The intersections of reinforcement fibers located in the membrane bulk are also observed on the pristine (Fig. 2a) and operated (Fig. 2b) anode's surfaces, enabling a precise nano-electrical and nanomechanical investigation of the anode depending on reinforcement fiber positions later-on. Both images show the alternating pattern of the vertically and horizontally oriented reinforcement fibers at intersections, that are located as web-woven structure underneath the anode. The intersecting fiber closer to the anode determines the visible orientation. Additionally, the operated anode, shown in Fig. 2b, exhibits features that are related to the utilized expanded metal grid PTL. Typical expanded metal grid structures are shown in Fig. S1.†[49,56] X-like areas are associated with a direct PTL interface, while the triangular-like areas are associated with PTL channel interfaces during electrolysis. Typically, one side of each PTL interface area shows a more prominent mark appearing like a slightly bowed line.

3.3 Nanomechanics

To evaluate the nanomechanics of the specific domains, described in Fig. 2, nanoindentations were performed spatially resolved on a pristine and an operated anode. It was found that

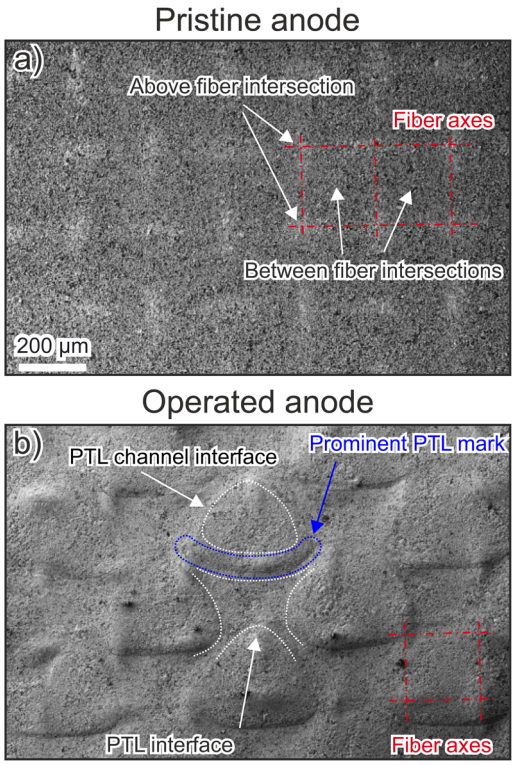

Fig. 2 (a) The SEM image of the pristine anode exhibits the anode surface with underlying reinforcement fiber intersections. The red dashed lines indicate the axis of underlying fibers. (b) Additionally, the SEM image of the operated anode exhibits specific features, that are associated with the expanded metal grid PTL features. Typical expanded metal grid structures are shown in Fig. S1.† Domains labelled as PTL interface are associated with a direct PTL contact, while PTL channel interface domains are associated with feed water contact during electrolysis. Furthermore, a prominent PTL mark on the anode at one side of each PTL interface is observed.

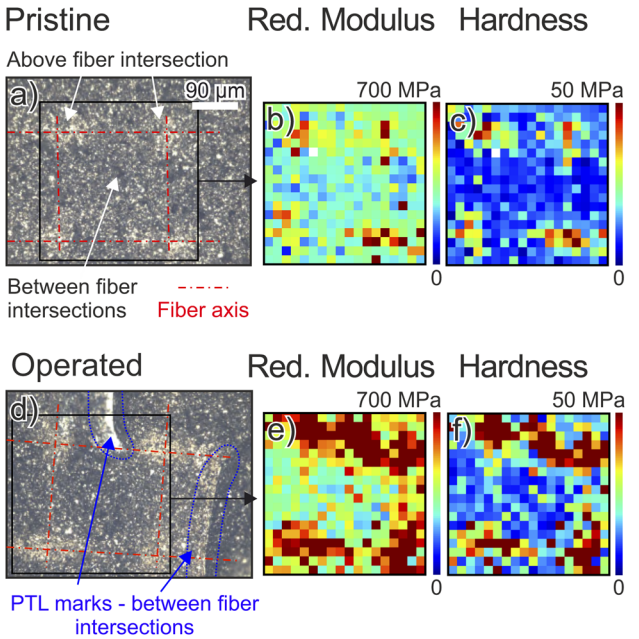

Fig. 3 (a) The optical microscope image of a pristine anode surface exhibits the location of the underlying web-woven reinforcement fiber intersections. The black box indicates the nanoindented area. (b) The reduced modulus map shows higher values in the vicinity of the reinforcement fiber intersections. (c) The hardness map shows a qualitatively similar result as the respective reduced modulus map. (d) The optical microscope image of the operated anode exhibits, additional to the underlying reinforcement fiber intersections, PTL marks between the upper two reinforcement fiber intersections and one on the right side, outside of the indented area. (e) The reduced modulus map of the operated anode exhibits increased values above the reinforcement fiber intersections, and additionally increased values at the PTL mark. (f) The hardness map shows qualitatively comparable results than the respective reduced modulus map. All 360 µm × 360 µm maps consist of equally distanced 18 × 18 indents performed with a maximum load of 800 µN resulting in indentation depths of a few µm. Data of the white point in (b) and (c) is not available.

the mean anode's reduced modulus and hardness increase with operation and are further locally increased if there are underlying reinforcement fiber intersections. PTL interface and PTL channel interface areas are not clearly distinguishable, while at PTL marks a significant increase in reduced modulus and hardness is observed.

Fig. 3a shows an optical microscope image of the pristine anode. The reinforcement fiber intersections in the bulk, such as displayed in the cross section (Fig. 1a) are observed in each corner of the image.

Fig. 3b shows the respective 360 µm × 360 µm nanoindentation map, that is acquired at the area indicated by the black box in Fig. 3a. In the vicinity of reinforcement fiber intersections, a higher reduced modulus is observed. The respective hardness map, displayed in Fig. 3c, exhibits a comparable trend.

The optical microscope image of the operated anode, shown in Fig. 3d, also exhibits intersections of the underlying reinforcement fibers in each corner. Additionally, one PTL mark is observed between the two fiber intersections on the top and one on the right, outside of the indented area indicated by the black box. In contrast to the SEM images (Fig. 2), the PTL interface area is not clearly distinguishable from the PTL channel interface area, while the prominent PTL mark is well visible in the optical microscope and the nanoindentation maps. Fig. 3e, shows a higher reduced modulus around the reinforcement fiber intersections stretching over a larger area compared to the pristine sample. Reinforcement fibers on the operated reduced modulus map might be more pronounced compared to the pristine map due to a thinner anode or membrane at these spots. While thinning might occur upon operation, local thickness variations might have already been present on the pristine sample. Furthermore, a high reduced modulus is observed at the PTL mark between the top fiber intersections. Similarly, the hardness map in Fig. 3f indicates an increased hardness around the reinforcement fiber intersections and additionally, around the PTL mark between the top fibers. The change in mechanical properties at the PTL mark indicates a significant structural or compositional change.

The in-depth nanoindentation analysis of a selective anode position, shown in Fig. 3, is extended by the analysis of multiple other positions across the pristine and operated anodes

(see Fig. S2†). The results, displayed in Fig. 4, clearly show that incorporated reinforcement fibers locally increase the hardness and the reduced modulus. The operated anode became more heterogeneous. Strikingly, around the PTL marks the most significant increase in mean hardness and mean reduced modulus is observed, highlighting the structural or compositional change of the anode layer at such spots. Subsequently, the details about the evaluation are given.

The indents of each nanoindentation map were categorized into different domains depending on the position of reinforcement fiber intersections and PTL mark positions. More details on the domain categorization are displayed in Fig. S3–S5.† The mean hardness and reduced modulus values of the same domain types were averaged across multiple positions and are shown in Fig. 4. In general, the results are in the same range as nanoindentation results from MEA catalysts layers reported in literature.[57–59] Domains above reinforcement fiber intersections show a higher mean reduced modulus (Fig. 4a) compared to positions between reinforcement fiber intersections. Low statistical deviations for the pristine anode indicate the high degree of homogeneity for each domain. The anode became more heterogeneous with operation as shown by the large statistical deviations. Compared to the pristine anode, the mean reduced modulus above and between reinforcement fiber intersections slightly increased. However, the statistical deviations indicate spots with lower hardness or reduced modulus compared to the pristine sample, which might be due to void formations inside the MEA,[60] or due to a locally significantly thinned or detached catalyst layer.[1] Furthermore, domains associated with the prominent PTL mark show the highest mean reduced modulus. PTL marks, that are above fiber intersections show a clearly higher reduced modulus compared to pristine positions, and likely an even higher reduced modulus than other operated domains without PTL marks.

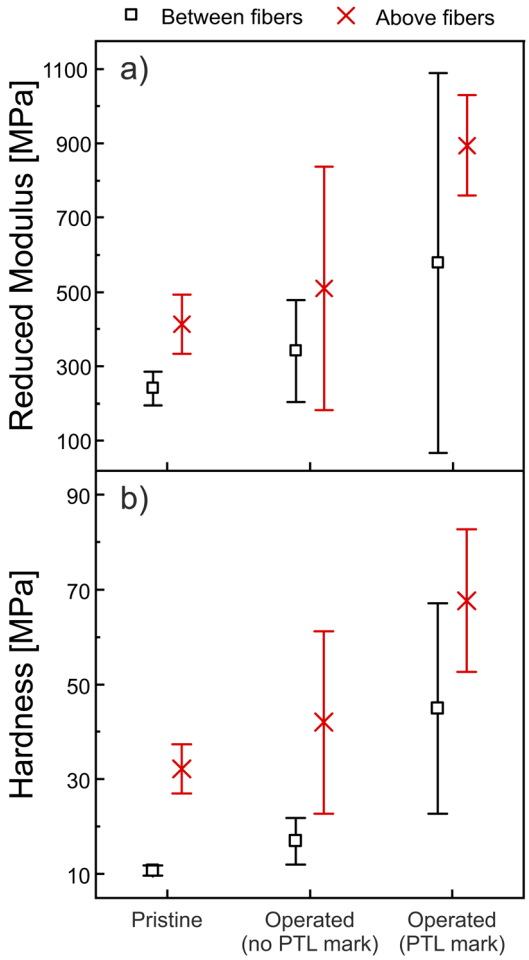

Fig. 4 (a) The mean reduced modulus of different domains across multiple anode positions is presented for the pristine and operated anode. Values are higher above reinforcement fiber intersections and for the operated anode. The operated anode heterogenized, indicated by large statistical deviations of the domains and the occurrence of additional PTL marks. (b) The mean hardnesses exhibit a similar trend as the reduced moduli. The prominent PTL marks were clearly identifiable with the nanoindenters optical microscope, while PTL channel and PTL interface areas were not clearly distinguishable and are therefore displayed as average labelled as 'operated – no PTL mark'. The mean values were calculated with indents segmented into the different domains (Fig. S5†) from 360 μm × 360 μm nanoindentation maps of four pristine and eight operated nanoindentation maps. Each data point includes at least 70 individual indents from at least 4 different positions.

In different measurements, the indenter probe centering above reinforcement fiber intersections might have slight offsets due to the 20 μm indent spacing. Thus, increased statistical deviations at such spots might result. Moreover, at anode positions without PTL marks, the statistical deviations might be higher because PTL and PTL channel interfaces are averaged as these are not clearly distinguishable with the nanoindenter optical microscope.

The hardness analysis, shown in Fig. 4b, yields qualitatively similar results as the reduced modulus analysis, shown in Fig. 4a. The mean hardness increases with operation, with the highest increase at the PTL marks. The hardness statistical deviations of the different domains exhibit less overlap compared to the reduced modulus results and thereby, clearly show that the domains differ in their nanomechanical properties underlining the importance of the PTL-anode interplay history during electrolysis.

The MEA's nanomechanical response is an interplay of catalyst particles, ionomer binder, pores, ionomer membrane, and reinforcement fibers. Thus, multiple mechanisms might contribute to the generally increased hardness and stiffness upon operation. First, a loss of soft and lower-stiffness ionomer within the anode might alter the nanomechanical behaviour, causing it to more align with the mechanical response of harder and stiffer catalyst. Second, MEA densification due to compaction of the MEA,[61] especially at PTL contacts,[62] increases the load-bearing cross section area, and thus might increase hardness and stiffness. Third, the ionomer's structure is reported to change upon hydration and induced current during electrolysis.[37,39,63] This effect might alter the nanomechanical response as well to a yet not investigated extent. While reported Ir catalyst dissolution,[45,64] is expected to rather reduce hardness and stiffness, recent reports highlight the possible agglomeration of

Ir at certain spots,[50,65] which might lead to a locally elevated hardness and stiffness.

As the nanoindentation results indicate a structural or compositional change of the anode bulk, PF-TUNA was performed to verify, if a nanomechanical change also occurs on the anode surface. In contrast to the nanoindentation maps of 360 μm × 360 μm, which were acquired with an indentation depth of a few μm, the PF-TUNA results were derived from 5 μm × 5 μm maps, that were acquired with an indentation depth of only a few nm. As the anode layer consists of Ir catalyst particles and ionomer, the PF-TUNA resolves the distribution of these species on the surface by analyzing their nanomechanical and nanoelectrical properties. Quantitative analysis reveals an increase in the catalyst particle stiffness with operation. To obtain these results, first the qualitative appearance of the PF-TUNA maps is described, and second, the quantitative analysis of such maps is elaborated.

Fig. 5a–c show an exemplary scan of a pristine anode surface located above a reinforcement fiber intersection. The topography, shown in Fig. 5a, exhibits particle agglomerates and a few plateau-like structures. The respective stiffness map, shown in Fig. 5b, shows low stiffness areas, *e.g.* in the bottom middle area. The respective contact current map (Fig. 5c) exhibits the electrically insulating nature of this low stiffness areas, while other parts are electrically conductive. The magnified scan, shown in Fig. 5e and f, underlines the presence of distinct species on the surface. A few high stiffness particles are observed, although not all of them exhibit measurable electrical currents. The matrix surrounding these particles exhibits a low stiffness, while another area at the bottom right of the image exhibits even lower stiffness. Both of these low stiffness areas correspond to the electrically non-conductive areas in the contact current map.

The high stiffness and electrically conductive particles indicate the presence of Ir catalyst. High stiffness catalyst particles, that are electrically non-conductive, are present due to two possible reasons: either there is a thin insulating ionomer film surrounding the particle's surface, or there is no electron percolation path to the bulk catalyst particles. The low modulus and electrically non-conductive areas are associated with ionomer. Fig. 5g shows a 3D representation of the PF-TUNA maps, displayed in Fig. 5d–f, to underline the spatial correlation of stiffness and contact current. The 3D structure of the topography map has the stiffness map as overlay. Furthermore, the white striped areas display the electrically conductive particles, on which a contact current above background noise was observed (10 pA).

For statistical analysis of the in-depth PF-TUNA results shown in Fig. 5, six individual PF-TUNA stiffness maps across the anode were evaluated for each domain—above and between fiber intersections and additionally with respect to visible PTL marks for the operated anode (see Fig. S7–S12†). This categorization of different domains aligns with the categorization for the nanoindentation results, utilizing the AFM optical microscope as allocation tool. More details about the analyzed positions are displayed in Fig. S2.†

Fig. 6a shows a histogram of the previously discussed examplary 5 μm × 5 μm stiffness map of the pristine anode (Fig. 5b). The peak deconvolution reveals two small peaks, one located around 20 MPa, and another located around 80 MPa. A larger peak is observed at around 100 MPa. As the large peak includes the high stiffness spots and mostly the electrically

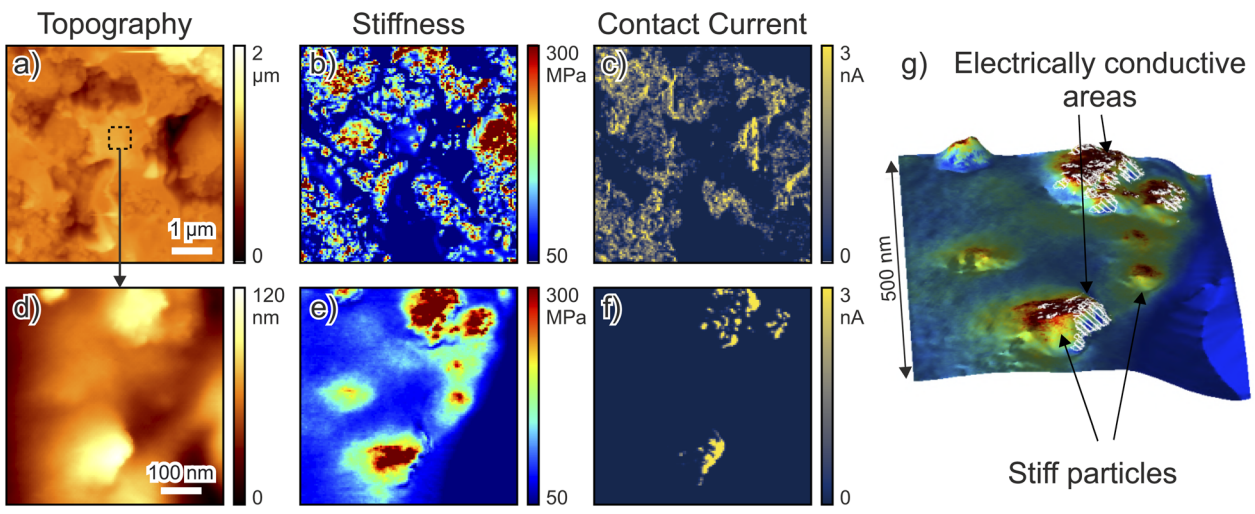

Fig. 5 (a) The topography of the pristine anode surface above an underlying reinforcement fiber intersection exhibits particle agglomerates and plateau-like structures. (b) The respective stiffness map reveals high stiffness surface areas embedded in a low stiffness surrounding matrix. (c) The corresponding contact current map exhibits electrically conductive and non-conductive areas. (d) The magnified topography was acquired at the area indicated by the dashed box in (a). (e) The respective magnified stiffness map exhibits the nanoscale distribution of high stiffness catalyst particles and low stiffness surrounding ionomer. (f) While the respective contact current map shows the electrically non-conductive nature of the ionomer, the catalyst particles are partly electrically conductive. High stiffness but electrically non-conductive domains are associated with catalyst particles with missing percolation paths to the voltage source or particles with a covering insulating ionomer layer. (g) The 3D map shows the 3D topography (d) with the stiffness (e) as skin overlay. White striped areas indicate electrically conductive areas with observed currents above background noise (10 pA).

conductive areas (see Fig. S6†), it is associated with the catalyst particles. As described in Fig. 6, the lower modulus areas are associated with the ionomer. The sharp peak 2, which is associated with the ionomer, is only observed at some pristine positions (see Fig. S8a–c†) and not at operated (Fig. S9–S12†). Therefore, to enable a quantitative and comprehensive comparison of pristine and operated samples, only the as catalyst associated peak is utilized. Such a catalyst peak is observed at all pristine and operated positions. Fig. 6b show the catalyst peak positions that were derived from multiple stiffness map histograms acquired across the anode. The catalyst peaks of the pristine anode's surface are located around 126 ± 67 MPa and 141 ± 60 MPa between and above reinforcement fiber intersections, respectively. Therefore, no clear difference is observed depending on the location of the underlying reinforcement fiber intersections. Analysis of the operated sample indicates a high statistical deviation across the sample. Averaged catalyst peak positions at PTL marks are located at 244 ± 80 MPa and 336 ± 115 MPa between and above fiber intersections, respectively. The analysis of other operated spots yielded catalyst peak positions at 231 ± 114 MPa and 274 ± 36 MPa between and above fiber intersections, respectively. A stiffening with operation is observed.

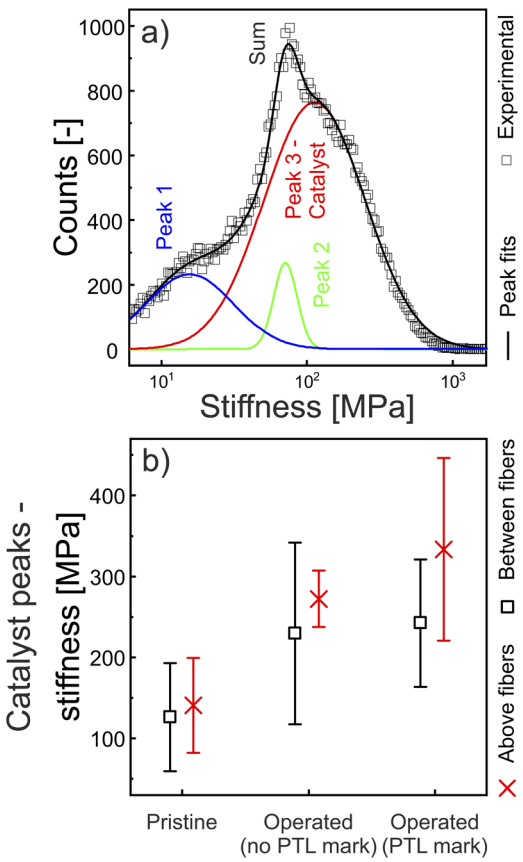

Fig. 6 (a) The stiffness histogram was derived from the 5 μm × 5 μm stiffness map, shown in Fig. 5b. The peak deconvolution ($R^2 = 0.995$) reveals two low stiffness peaks. A larger peak is associated with the catalyst, as it includes the high stiffness and electrically conductive pixels (Fig. S6†). (b) The stiffness histograms of maps acquired at multiple positions (see Fig. S2†) were deconvoluted and the averaged catalyst peaks are presented for the pristine and operated sample and its various domains (see Fig. S3 and S4†). The average catalyst stiffness increases with operation. The operated anode surface exhibits a more heterogeneous stiffness, shown by the statistical deviations.

As the measured stiffness rather resembles those of typical PFSA ionomers,[66,67] and not of iridium,[68] the ionomer or underlying pores dominate the anode's nanomechanical response. Statistical deviations might be related to local variations of pore sizes and ionomer layer thickness, that surround the catalyst particles. In contrast to the nanoindentation results, the influence of underlying reinforcement fibers is not clearly observable in the nanomechanical PF-TUNA results. The mean catalyst peak positions above reinforcement fiber intersections are only slightly higher above compared to spots between reinforcement fiber intersections, with overlapping statistical deviations. As the PF-TUNA tip indents only a few nm, the influence of the several μm deep fibers is less observable, compared to the nanoindentation experiments. At PTL positions above reinforcement fiber intersections the highest mean stiffness is observed, which is also observed in the nanoindentation results. The interplay of reinforcement fibers and PTL might lead to a different contact during electrolysis compared to other spots, which might result in a locally increased aging.

The PF-TUNA results indicate an increasing mean stiffness with operation, as already indicated by the nanoindentation results in Fig. 4. Therefore, the topmost nm of the anode surface may contribute to the results acquired by the μm deep nanoindentations. The stiffening of the catalyst might be promoted by a thinning of the covering or underlying ionomer that entangles the catalyst particles, and contributes to the local mechanical properties of the composite material. Ionomer thinning is already reported in the literature.[23] Moreover, the stiffening and hardening shown by nanoindentation results might also be promoted by stiff contaminations, which are partially observed at PF-TUNA stiffness histograms of the operated anode (*e.g.* Fig. S9e†). Energy dispersive spectroscopy (EDS) analysis hints at traces of Ti and Fe contaminants (Fig. S13†) on the operated sample. While the Ti most likely originates from the PTL, the Fe might originate from the feed water which is in contact with the piping or other process related components.[1,69]

3.4 Nanoelectrics

After quantifying and statistically analyzing the nanomechanical PF-TUNA results, herein, the simultaneously acquired contact current maps are evaluated. Thus, a more complete insight into the anode surface composition is provided. The observed increase in electrically conductive surface area with operation is discussed in the following.

Fig. 7 shows the statistical analysis of the 5 μm × 5 μm contact current maps. The conductive surface area fraction indicates the fraction of pixels, at which a contact current above background noise (10 pA) is observed. The average conductive surface area fraction is higher between compared to above reinforcement fiber intersections. The pristine sample exhibits

the least conductive surface area fraction with 50 ± 2%, and 62 ± 13% for positions above and between fiber intersections respectively. With operation the conductive surface area fraction at positions without PTL marks increased to 68 ± 10% and 84 ± 6% above and between fiber intersections, respectively. The mean conductive surface area fraction is the highest at the PTL marks with 89 ± 8% and 93 ± 6% for positions above and between fiber intersections respectively.

An increase in conductive surface area fraction is in agreement with literature.[43] In a PEM electrolysis degradation study, the authors show an increase of conductive surface area fraction of around 50% on the anode after degradation. The authors associate this increase with a loss of electrically non-conductive ionomer-rich areas. Herein, a decrease of ionomer with operation is additionally in line with the stiffness results. The operated samples' stiffness histograms reveal no sharp peaks (Fig. S9–S12†), that are associated with the ionomer (such as in Fig. 6a). Another reason for an increase of conductive surface area fraction might be a loss of ultrathin ionomer films that surround the catalyst particles and prevent electron percolation paths to the subsurface bulk catalyst for the pristine samples. Such a thinning of the ultrathin ionomer film was shown already for PEMFCs.[23] Thereby, new electrical percolation paths to previously non-contacted surface catalyst particles might form. EDS data (Fig. S13†) underlines the vast Ir (catalyst) and F (ionomer) concentration on the operated anode, highlighting that mostly Ir contributes to the electrical signal. Contaminants are only found to a small extent. While contaminants were reported as cations at ion exchange sites of the ionomer,[1] the presence of contaminants as solid agglomerates might be indicated by high stiffness peaks in the histograms (*e.g.* Fig. S9e or S11b and d†). The electrical analysis of such high stiffness peaks indicate the possibility of both: high stiffness electrically conductive contaminants (*e.g.* Fig. S11d†) or high stiffness electrically non-conductive contaminants (*e.g.* Fig. S9e†).

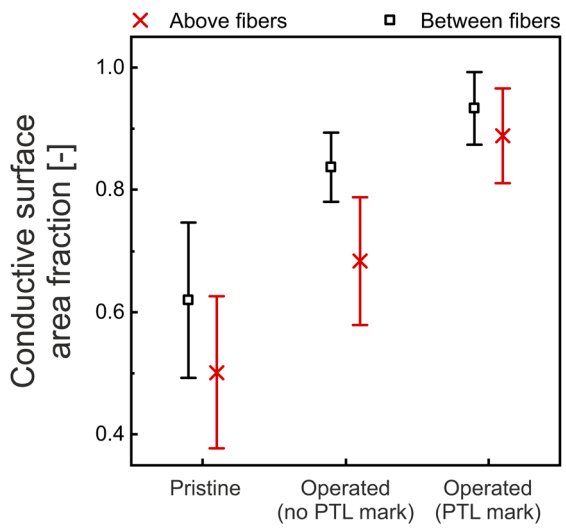

Fig. 7 The conductive surface area fraction of an individual contact current map indicates the fraction of pixels with a contact current above background noise (10 pA). With operation, the mean values increased. The highest conductive surface area fractions are observed at the PTL marks. The results of six 5 μm × 5 μm contact current maps were averaged for each data point, except for the domains between reinforcement fiber intersections at PTL marks, where one contact current map was left out due to a general missing electrical contact (Fig. S9b†).

Lastly, the in Fig. 7 observed influence of reinforcement fibers is discussed. Locations between reinforcement fiber intersections show an increased mean conductive surface area fraction compared to locations above reinforcement fiber intersections for the operated and pristine anodes. The difference at PTL marks becomes small, as the conductive surface area fraction approaches 100%. A reason might be the varying mechanical, conductive, or swelling properties of the bulk reinforcement fibers, which lead to different electrical surface properties after manufacturing or which further influence the catalyst properties during operation.

4 Conclusion

There is an urgent need to optimize PEMEC MEAs for competitive electrochemical hydrogen production, requiring the analysis of long-term operated MEAs. Through nano-electrical and nanomechanical analysis of pristine and operated web-woven fiber reinforced MEAs significant insights into their longevity have been gained.

The web-woven reinforcement fibers improve the local nanomechanical properties of the MEA and mitigate critical membrane failure over a long-term operation of more than 5000 h. Interestingly both, pristine and operated anodes exhibit a slightly diminished electrically conductive surface area above reinforcement fiber intersections indicating a potential fiber influence on the nanoelectrics. The pristine anode exhibits homogeneous nanomechanical properties on a large scale with variations only arising at specific points where reinforcement fiber intersections are located. With operation, an increase of reduced modulus and hardness is observed. The increase is likely promoted by a loss of low stiffness and soft ionomer in the catalyst layer, which is indicated by the AFM stiffness histogram analysis and the large observed fraction of electrically conductive surface area on the operated anode. Moreover, operated anode analysis reveals varying domains depending on the PTL expanded metal grid contact history. While PTL and PTL channel interface areas remained largely indistinguishable, a strikingly high increase of reduced modulus, hardness and conductive surface area is systematically observed at prominent PTL marks, located at one side of each PTL and PTL channel interface area.

The question is raised if structural or compositional change mostly occurred at these comparably small PTL marks, because the PTL had only significant contact at these spots or because the direct additional interface to a PTL channel plays a crucial role. Furthermore, contributions of ionomer loss and catalyst dissolution/reprecipitation to the observed structural or compositional changes are of interest for future research. Moreover, it is important to evaluate how these alterations impact the macroscopic behavior, potentially leading to hot-spot formation or passivated areas that could affect efficiency or provoke MEA failures.

Data availability

Data for this article, including AFM and nanoindentation data, are available at Jülich DATA at **https://doi.org/10.26165/JUELICH-DATA/IFMKQU**.

Conflicts of interest

There are no conflicts to declare.

Acknowledgements

The authors gratefully acknowledge the financial support by the German Federal Ministry of Education and Research (BMBF) within the H2Giga project DERIEL (grant number 03HY122C). Furthermore, the authors delightedly thank Sebastian Lehmann for the 3D model and schematics of the reinforcement fiber mesh.

Notes and references

1 Q. Feng, X.-Z. Yuan, G. Liu, B. Wei, Z. Zhang, H. Li and H. Wang, *J. Power Sources*, 2017, **366**, 33–55.
2 W. Li, Y. Bu, X. Ge, F. Li, G.-F. Han and J.-B. Baek, *ChemSusChem*, 2024, e202400295.
3 C. Wang, F. Lan, Z. He, X. Xie, Y. Zhao, H. Hou, L. Guo, V. Murugadoss, H. Liu, Q. Shao, Q. Gao, T. Ding, R. Wei and Z. Guo, *ChemSusChem*, 2019, **12**, 1576–1590.
4 J. Li, W. Tian, Q. Li and S. Zhao, *ChemSusChem*, 2024, e202400239.
5 F. N. Khatib, T. Wilberforce, O. Ijaodola, E. Ogungbemi, Z. El-Hassan, A. Durrant, J. Thompson and A. G. Olabi, *Renewable Sustainable Energy Rev.*, 2019, **111**, 1–14.
6 S. Stucki, G. Scherer, S. Schlagowski and E. Fischer, *J. Appl. Electrochem.*, 1998, **28**, 1041–1049.
7 P. Millet, A. Ranjbari, F. De Guglielmo, S. A. Grigoriev and F. Auprêtre, *Int. J. Hydrogen Energy*, 2012, **37**, 17478–17487.
8 F. Andolfatto, R. Durand, A. Michas, P. Millet and P. Stevens, *Int. J. Hydrogen Energy*, 1994, **19**, 421–427.
9 M. Chandesris, V. Médeau, N. Guillet, S. Chelghoum, D. Thoby and F. Fouda-Onana, *Int. J. Hydrogen Energy*, 2015, **40**, 1353–1366.
10 H. Liu, F. D. Coms, J. Zhang, H. A. Gasteiger and A. B. LaConti, *Polymer Electrolyte Fuel Cell Durability*, 2009, pp. 71–118.
11 S. Grigoriev, P. Millet, S. Volobuev and V. Fateev, *Int. J. Hydrogen Energy*, 2009, **34**, 4968–4973.
12 Y. Kobayashi, K. Kosaka, T. Yamamoto, Y. Tachikawa, K. Ito and K. Sasaki, *Int. J. Hydrogen Energy*, 2014, **39**, 16263–16274.
13 F. Lapicque, M. Belhadj, C. Bonnet, J. Pauchet and Y. Thomas, *J. Power Sources*, 2016, **336**, 40–53.
14 P. Shirvanian and F. van Berkel, *Electrochem. Commun.*, 2020, **114**, 106704.
15 F. Liu, B. Yi, D. Xing, J. Yu and H. Zhang, *J. Membr. Sci.*, 2003, **212**, 213–223.
16 T. R. Ralph, D. E. Barnwell, P. J. Bouwman, A. J. Hodgkinson, M. I. Petch and M. Pollington, *J. Electrochem. Soc.*, 2008, **155**, B411.
17 C. J. Linnartz, A. Rommerskirchen, J. Walker, J. Plankermann-Hajduk, N. Köller and M. Wessling, *J. Membr. Sci.*, 2020, **605**, 118095.
18 A. Kusoglu and A. Z. Weber, *Chem. Rev.*, 2017, **117**, 987–1104.
19 S. Auffarth, W. Dafinger, J. Mehler, V. Ardizzon, P. Preuster, P. Wasserscheid, S. Thiele and J. Kerres, *J. Mater. Chem. A*, 2022, **10**, 17208–17216.
20 J. Kink, M. Ise, B. Bensmann, P. Junker and R. Hanke-Rauschenbach, *J. Electrochem. Soc.*, 2023, **170**, 114513.
21 Y. Xing, L. Liu, Z. Fu, Y. Li and H. Li, *Int. J. Hydrogen Energy*, 2024, **50**, 79–90.
22 T. Morawietz, M. Handl, C. Oldani, K. A. Friedrich and R. Hiesgen, *Fuel Cells*, 2018, **18**, 239–250.
23 T. Morawietz, M. Handl, C. Oldani, P. Gazdzicki, J. Hunger, F. Wilhelm, J. Blake, K. A. Friedrich and R. Hiesgen, *J. Electrochem. Soc.*, 2018, **165**, F3139–F3147.
24 S. Siracusano, F. Pantò, S. Tonella, C. Oldani and A. S. Aricò, *Int. J. Hydrogen Energy*, 2022, **47**, 15557–15570.
25 S. Giancola, M. Zatoń, Á. Reyes-Carmona, M. Dupont, A. Donnadio, S. Cavaliere, J. Rozière and D. J. Jones, *J. Membr. Sci.*, 2019, **570**, 69–76.
26 H.-Y. Li and Y.-L. Liu, *J. Mater. Chem. A*, 2013, **1**, 1171–1178.
27 M. Cieluch, D. Düerkop, N. Kazamer, F. Wirkert, P. Podleschny, U. Rost, A. Schmiemann and M. Brodmann, *Int. J. Hydrogen Energy*, 2024, **52**, 521–533.
28 Y. Kai, Y. Kitayama, M. Omiya, T. Uchiyama and M. Kato, *J. Fuel Cell Sci. Technol.*, 2013, **10**(2), 021007.
29 X. Huang, R. Solasi, Y. Zou, M. Feshler, K. Reifsnider, D. Condit, S. Burlatsky and T. Madden, *J. Polym. Sci., Part B:Polym. Phys.*, 2006, **44**, 2346–2357.
30 J. Kink, M. Ise, B. Bensmann and R. Hanke-Rauschenbach, *J. Electrochem. Soc.*, 2023, **170**, 054507.
31 M. R. VanLandingham, J. S. Villarrubia, W. F. Guthrie and G. F. Meyers, *Macromol. Symp.*, 2001, 15–44.
32 R. Xia, H. Zhou, R. Wu and W.-P. Wu, *Polymers*, 2016, **8**(9), 344.
33 E. A. Franceschini and H. R. Corti, *J. Power Sources*, 2009, **188**, 379–386.
34 S. Du, S. Guan, S. Mehrazi, F. Zhou, M. Pan, R. Zhang, P.-Y. A. Chuang and P.-C. Sui, *J. Electrochem. Soc.*, 2021, **168**, 114506.
35 J. Hyun, S. Hwan Yang, D. Wook Lee, E. Oh, H. Bae, M. Suc Cha, G. Doo, J. Yong Lee and H.-T. Kim, *Chem. Eng. J.*, 2023, **469**, 143919.
36 R. Hiesgen, S. Helmly, I. Galm, T. Morawietz, M. Handl and K. A. Friedrich, *Membranes*, 2012, **2**, 783–803.
37 R. Hiesgen, S. Helmly, T. Morawietz, X.-Z. Yuan, H. Wang and K. A. Friedrich, *Electrochim. Acta*, 2013, **110**, 292–305.
38 R. Hiesgen, T. Morawietz, M. Handl, M. Corasaniti and K. A. Friedrich, *J. Electrochem. Soc.*, 2014, **161**, F1214–F1223.
39 R. Hiesgen, T. Morawietz, M. Handl, M. Corasaniti and K. Friedrich, *Electrochim. Acta*, 2015, **162**, 86–99.

40 F. Mack, M. Klages, J. Scholta, L. Jörissen, T. Morawietz, R. Hiesgen, D. Kramer and R. Zeis, *J. Power Sources*, 2014, **255**, 431–438.
41 T. Morawietz, M. Handl, C. Oldani, K. A. Friedrich and R. Hiesgen, *ACS Appl. Mater. Interfaces*, 2016, **8**, 27044–27054.
42 T. Morawietz, M. Handl, M. Simolka, K. A. Friedrich and R. Hiesgen, *ECS Trans.*, 2015, **68**, 3–12.
43 P. Lettenmeier, L. Wang, U. Golla-Schindler, P. Gazdzicki, N. A. Cañas, M. Handl, R. Hiesgen, S. S. Hosseiny, A. S. Gago and K. A. Friedrich, *Angew. Chem.*, 2016, **128**, 752–756.
44 C. Liu, M. Shviro, G. Bender, A. S. Gago, T. Morawietz, M. J. Dzara, I. Biswas, P. Gazdzicki, Z. Kang, S. F. Zaccarine, S. Pylypenko, K. A. Friedrich, M. Carmo and W. Lehnert, *J. Electrochem. Soc.*, 2023, **170**, 034508.
45 H. Yu, L. Bonville, J. Jankovic and R. Maric, *Appl. Catal., B*, 2020, **260**, 118194.
46 J. Borowec, V. Selmert, A. Kretzschmar, K. Fries, R. Schierholz, H. Kungl, R.-A. Eichel, H. Tempel and F. Hausen, *Adv. Mater.*, 2023, 2300936.
47 K. Xu, W. Sun, Y. Shao, F. Wei, X. Zhang, W. Wang and P. Li, *Nanotechnol. Rev.*, 2018, **7**, 605–621.
48 S. Stiber, N. Sata, T. Morawietz, S. A. Ansar, T. Jahnke, J. K. Lee, A. Bazylak, A. Fallisch, A. S. Gago and K. A. Friedrich, *Energy Environ. Sci.*, 2022, **15**, 109–122.
49 S. S. Lafmejani, M. Müller, A. C. Olesen and S. K. Kær, *J. Power Sources*, 2018, **397**, 334–342.
50 C. Heume, V. Karyofylli, A. Javed, K. Dzieciol, S. Basak, J.-P. Poc, Y. Tasdemir, Y. Rutsch, L. Rein, N. Wolf, *et al.*, *Research Square*, 2024, preprint, DOI: 10.21203/rs.3.rs-5337119/v1.
51 Y. Katayanagi, T. Shimizu, Y. Hashimasa, N. Matsushita, Y. Yamazaki and T. Yamaguchi, *J. Power Sources*, 2015, **280**, 210–216.
52 W. C. Oliver and G. M. Pharr, *J. Mater. Res.*, 1992, **7**, 1564–1583.
53 B. V. Derjaguin, V. M. Muller and Y. P. Toporov, *J. Colloid Interface Sci.*, 1975, **53**, 314–326.
54 T. J. Young, M. A. Monclus, T. L. Burnett, W. R. Broughton, S. L. Ogin and P. A. Smith, *Meas. Sci. Technol.*, 2011, **22**, 125703.
55 O. Scholder, *Scholi/pySPM v0.2.20*, 2019, DOI: 10.5281/zenodo.2650457, accessed: January 2023.
56 E. Hoppe, S. Holtwerth, M. Müller and W. Lehnert, *J. Power Sources*, 2023, **578**, 233242.
57 K. Poornesh, C. Cho, G. Lee and Y. Tak, *J. Power Sources*, 2010, **195**, 2709–2717.
58 K. Poornesh and C. Cho, *Int. J. Hydrogen Energy*, 2011, **36**, 3623–3634.
59 Y. Shen, Mechanical degradation of membrane electrode assemblies in proton exchange membrane fuel cells, PhD thesis, University of Waterloo, Canada, 2017.
60 S. Tsushima and S. Hirai, *J. Therm. Sci. Technol.*, 2015, **10**, JTST0002.
61 F. Aldakheel, C. Kandekar, B. Bensmann, H. Dal and R. Hanke-Rauschenbach, *Comput. Methods Appl. Mech. Eng.*, 2022, **400**, 115580.
62 K. J. Ferner, J. Park, Z. Kang, S. A. Mauger, M. Ulsh, G. Bender and S. Litster, *Int. J. Hydrogen Energy*, 2024, **59**, 176–186.
63 M. Bass, A. Berman, A. Singh, O. Konovalov and V. Freger, *J. Phys. Chem. B*, 2010, **114**, 3784–3790.
64 M. Burch, K. Lewinski, M. Buckett, S. Luopa, F. Sun, E. Olson and A. Steinbach, *J. Power Sources*, 2021, **500**, 229978.
65 M. Stähler, A. Burdzik, I. Friedrich, A. Everwand and F. Scheepers, *Int. J. Hydrogen Energy*, 2024, **78**, 682–687.
66 A. Kusoglu, Y. Tang, M. Lugo, A. M. Karlsson, M. H. Santare, S. Cleghorn and W. B. Johnson, *J. Power Sources*, 2010, **195**, 483–492.
67 M. B. Satterfield and J. B. Benziger, *J. Polym. Sci., Part B:Polym. Phys.*, 2009, **47**, 11–24.
68 Y. Cerenius and L. Dubrovinsky, *J. Alloys Compd.*, 2000, **306**, 26–29.
69 S. Siracusano, N. van Dijk, R. Backhouse, L. Merlo, V. Baglio and A. S. Aricò, *Renewable Energy*, 2018, **123**, 52–57.